Theoretical study of dislocation emission around a nanoindentation using a static atomistic model

Yeau-Ren Jeng[1] and Chung-Ming Tan[2]
[1]*Department of Mechanical Engineering, National Chung Cheng University, Chia-Yi, Taiwan*
[2]*Department of Mechanical Engineering, WuFeng Institute of Technology, Chia-Yi, Taiwan*
(Received 22 July 2003; revised manuscript received 5 December 2003; published 24 March 2004)

This study uses an atomistic approach to simulate the emission of dislocations around a nanoindentation on a (001) copper surface. This approach is quasistatic, and is therefore computationally efficient. The simulation results illustrate the nucleation and emission of the dislocations. Slip vector analysis facilitates the observation of the dislocations and enables an interpretation of the dislocation reactions which are induced during the nanoindentation cycle. The results confirm that the von Mises shear stress is a good indicator of the atomic plastic behavior which occurs during the nanoindentation process.

DOI: 10.1103/PhysRevB.69.104109 PACS number(s): 62.20.Fe, 61.72.Bb, 68.35.Gy

INTRODUCTION

The continuing advances in nanotechnology require the development of some form of technique to determine the *in situ* mechanical behaviors of nanoscale materials. Previous studies have developed nanoindentation methods which enable the mechanical properties of a nanoscale material to be determined through an analysis of the load-depth curve generated during the nanoscale indentation cycle.[1–10] Furthermore, atomistic simulation methods are attracting increasing attention as a means of exploring the atomic processes involved in the nanoindentation process.[11–13]

Zimmerman *et al.*[11] used atomistic simulations to elucidate the effects of surface steps upon the nanoindentation process, and determined that the yielding load decreases when the nanoindentation takes place in close proximity to the step. Meanwhile, Fuente *et al.*[12] used scanning tunneling microscopy and atomistic simulations to investigate the emission of dislocation loops around a nanoindentation. In their study, the dislocation loops which are observed experimentally were reproduced by means of simulation. Finally, Gannepalli *et al.*[13] performed atomistic studies to investigate the nucleation and evolution of dislocations during the nanoindentation of a gold crystal. Their results confirmed that strain hardening of the indented surface is caused by the sessile dislocations which are generated by the zipping of the partials.

Although these studies adopted molecular-dynamics (MD) simulations to perform their investigations, this approach is very time-consuming since it involves time resolutions of a femto-second, or even less. Accordingly, the present study chooses to adopt an alternative approach, which resembles finite-element methodology (FEM) and is hence designated as the modified-FEM approach. Since it is known that atoms oscillate thermodynamically around their minimum-energy positions, the current approach calculates only the incremental changes of the minimum-energy positions which occur during the indentation process. In this way, the computation activity becomes quasistatic, which enables a significant reduction in the required computational time. In the present investigation, this modified-FEM approach is used to perform a qualitative simulation of the dislocation emissions around the area of nanoindentation on a (001) fcc copper surface. The distribution of the resulting stress and strain is then examined to clarify the atomic plastic behavior induced during the nanoindentation cycle.

METHODOLOGY

Figure 1(a) presents the simulation model employed to investigate the indentation of a perfect copper crystal surface by a rigid triangular pyramid diamond tip. In order that deformation of the indenter may be ignored within the simulation, an assumption is made that the hardness of the indenter's diamond tip is much greater than the hardness of the

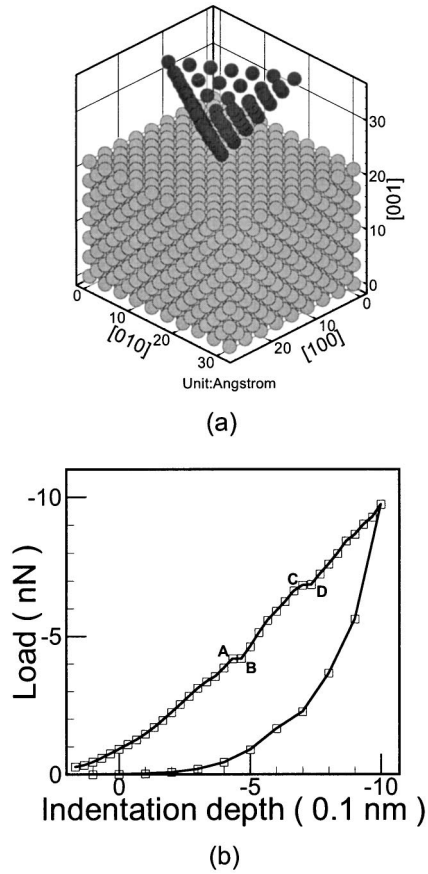

FIG. 1. (a) Atomic configuration of the indenter and the copper crystal. (b) Simulated load-depth curve for the complete nanoindentation cycle.

copper surface. Furthermore, a boundary condition is imposed which assumes that the atoms at the base of the copper crystal are fully constrained and the atoms on the outer surfaces normal to the base are free. The dimensions of the simulated crystal are 28 Å×32 Å×22 Å. Finally, the Morse potential is employed to model the interatomic pairwise potentials of the copper crystal. This potential function is given by

$$\phi(r_{ij})=D\{\exp[-2\alpha(r_{ij}-r_0)]-2\exp[-\alpha(r_{ij}-r_0)]\}, \tag{1}$$

where r_{ij} is the distance between atoms i and j, and the copper constants D, α, and r_0 are specified as 0.3429, 0.9545, and 2.7202, respectively.

Furthermore, the simulation adopts the Born-Mayer potential to model the interactions between the carbon and the copper atoms. This potential generates an impulsive force only, and is expressed as

$$\phi(r_{ij})=A\exp[-2\alpha(r_{ij}-r_0)], \tag{2}$$

where r_{ij} is the distance between carbon atom i and copper atom j, and the carbon/copper constants A, a, and r_0[14] are taken to be 0.3579 eV, 0.9545 Å^{-1}, and 2.5 Å, respectively.

A computationally efficient approach based on the nonlinear finite-element formulation is established by taking any two arbitrary atoms i and j as two nodes, and their potential as one element. It is assumed that the coordinates of atom i are (x_i,y_i,z_i) and that its displacements in the x, y, and z directions are given by u_i, v_i, and w_i, respectively. By defining the nodal displacement vector, $\{u\}_{ij}$, and the corresponding external nodal force vector, $\{F\}_{ij}=(f_i,g_i,h_i,f_j,g_j,h_j)^T$, for atoms i and j, the total pairwise potential energy can be expressed in the form

$$E_{ij}=\phi(r_{ij})-\{u\}_{ij}^T\{F\}_{ij}, \tag{3}$$

where the atomic distance r_{ij} is given by

$$r_{ij}=\{(x_i+u_i-x_j-u_j)^2+(y_i+v_i-y_j-v_j)^2+(z_i+w_i-z_j-w_j)^2\}^{1/2}, \tag{4}$$

such that its differential with respect to $\{u\}_{ij}$ is

$$dr_{ij}=[B]d\{u\}_{ij}. \tag{5}$$

Applying the principle of minimum work enforces the minimization of E_{ij} with respect to $\{u\}_{ij}$, i.e.,

$$\frac{\partial E_{ij}}{\partial\{u\}_{ij}}=\left(\frac{\partial\phi}{\partial r_{ij}}\right)[B]^T-\{F\}_{ij}=\{0\}. \tag{6}$$

It is noted that Eq. (6) is the element equilibrium equation and therefore represents the equilibrium of the various forces acting on atoms i and j. An unbalanced force $\{\xi\}_{ij}$ can be defined in the form

$$\{\xi\}_{ij}=\left(\frac{\partial\phi}{\partial r_{ij}}\right)[B]^T-\{F\}_{ij}. \tag{7}$$

The equilibrium equation is solved by means of an iterative procedure which continues until the equation converges to zero with an acceptable tolerance. In order to solve the nonlinear equilibrium equation using an iterative procedure, it is first necessary to differentiate $\{\xi\}_{ij}$ with respect to $\{u\}_{ij}$, i.e.,

$$\begin{aligned}d\{\xi\}_{ij}&=d\left(\frac{\partial\phi}{\partial r_{ij}}\right)[B]^T+\left(\frac{\partial\phi}{\partial r_{ij}}\right)d[B]^T\\&=[B]^T\left(\frac{\partial^2\phi}{\partial r_{ij}^2}\right)dr_{ij}+\left(\frac{\partial\phi}{\partial r_{ij}}\right)d[B]^T\\&=([K]_{ij}+[K_\sigma]_{ij})d\{u\}_{ij}=[K_T]_{ij}d\{u\}_{ij},\end{aligned} \tag{8}$$

where

$$[K]_{ij}=[B]^T\left(\frac{\partial^2\phi}{\partial r_{ij}^2}\right)[B] \tag{9}$$

and

$$[K_\sigma]_{ij}=\left(\frac{\phi}{r_{ij}}\right)\left[\frac{\partial[B]^T}{\partial u_i},\frac{\partial[B]^T}{\partial v_i},\frac{\partial[B]^T}{\partial w_i},\frac{\partial[B]^T}{\partial u_j},\frac{\partial[B]^T}{\partial v_j},\frac{\partial[B]^T}{\partial w_j}\right]. \tag{10}$$

Equation (9) can be solved by substituting Eq. (5) into the second line of Eq. (8). Subsequently, the conventional assembly procedure of the finite-element formulation is applied to assemble Eq. (8) in order to derive the total system equation, i.e,

$$d\{\xi\}=[K_T]d\{u\}. \tag{11}$$

Similarly, Eq. (7) can be assembled to derive the total system equilibrium equation, i.e.,

$$\sum_{i\neq j}\left(\frac{\partial\phi}{\partial r_{ij}}\right)[B]^T-\{F\}_{ij}=\{f\}_{\text{internal}}-\{F\}_{\text{external}}=\{0\}. \tag{12}$$

In terms of the finite-element formulation, Eq. (11) represents the tangent stiffness equation, while the terms $\{f\}_{\text{internal}}$ and $\{F\}_{\text{external}}$ in Eq. (12) denote the internal force vector and the external force vector, respectively. The Newton-Raphson iterative technique is applied to solve the total system equilibrium equation given in Eq. (12) using a suitable displace-

ment control scheme. In this iterative technique, it is assumed that the external force vector $\{F\}_{\text{external}}$ maintains a specified form during the iteration process, i.e.,

$$\{F\}^i = \{F\}^{i-1} + \lambda^i \{\hat{F}\}, \quad i = 1,2,..., \tag{13}$$

where $\{\hat{F}\}$ is the reference load vector.

If Eq. (13) is substituted into Eq. (11), the iterative tangent stiffness equation becomes

$$[K_T] d\{u\}^i = \lambda^i \{\hat{F}\} + d\{\xi\}^i, \quad i = 1,2,.... \tag{14}$$

Similarly, the iterative displacement increment can be expressed as

$$d\{u\}^i = \lambda^i \{u\}_a^i + d\{u\}_b^i, \quad i = 1,2,..., \tag{15}$$

where

$$\begin{aligned} [K_T]\{u\}_a^i &= \{\hat{F}\}, \\ [K_T] d\{u\}_b^i &= d\{\xi\}^i, \quad i = 1,2,.... \end{aligned} \tag{16}$$

Under the ''displacement'' control scheme, the qth component of the incremental displacement vector is maintained as a constant during the iteration process, i.e.,

$$\begin{aligned} \lambda^i u_{aq}^i + du_{bq}^i &= du_q^i \\ du_q^i &= \begin{cases} du_q, & i = 1 \\ 0, & i > 1 \end{cases}. \end{aligned} \tag{17}$$

The iterative solution strategy described above enables the derivation of the whole equilibrium path of the nanoindentation. Once the equilibrium path of each atom has been determined, the stress tensor at the atomic site can be determined in the following form:[15]

$$\sigma_{km}^i = \frac{1}{V^i} \sum_{j \neq i}^{N} f_k^{ij} r_m^{ij}, \tag{18}$$

where i refers to the atom in question, j denotes its neighboring atom, r_m^{ij} is a displacement vector from atom i to atom j, N is the total number of nearest-neighboring atoms, and V^i is the volume of the atom in question.

Meanwhile, the atomic strain tensor[13] is calculated as

$$E = \tfrac{1}{2}(D^T D - I), \tag{19}$$

where D is the deformation gradient defined as follows:

$$D = XY^{-1}, \tag{20}$$

$$X = \sum_{\beta}^{m} d_t^{\beta} \otimes d_\theta^{\beta}, \tag{21}$$

$$Y = \sum d_\theta^{\beta} \otimes d_\theta^{\beta}, \tag{22}$$

where d_t^{β} and d_θ^{β} are the vector differences of atom β and the atom in question positions at displacement step t and θ.

A slip vector, which is closely related to the Burgers vector, can be defined for each atom,[12] i.e.,

$$s = \frac{1}{n_s} \sum_{i=1}^{n_s} d_t^i - d_\theta^i, \tag{23}$$

where i refers to the nearest neighbors of the atom in question, n_s refers to the number of neighboring atoms which have slipped, and d_t^i and d_θ^i are vectors from the atom in question to the neighboring atom at steps t and θ, respectively. Conventionally, step θ indicates the step immediately prior to indentation, i.e., the point at which zero stress has been induced by the indenter.

RESULTS AND DISCUSSION

Figure 1(b) presents the simulated load-depth curve over the entire nanoindentation cycle, where the load reflects the force experienced by the indenter. By choosing to neglect the effects of atomic thermal vibration, this study transforms the MD formulation into a quasistatic finite-element structural approach. Therefore, the stability of the crystalline structure is correlated to, and can be monitored by, the positiveness of the modified-FEM tangent stiffness matrix. The irreversible plastic deformations observed in the simulation can be considered to arise from the changes in the crystalline structure caused by the instabilities induced by high localized stresses. The initial localized instability of the copper crystal structure is revealed in the load-depth curve by the reduced rate of slope increase noted between point *A* and point *B* in Fig. 1(b). It is noted that similar behavior is also observed during the simulation steps between point *C* and point *D*. The figure also indicates that the first pop-in consumes all the accumulated strain energy. Then of course new strain energy has to be built up, so the next pop-in is by necessity higher.

The stresses induced in the copper crystal as the indenter attains its maximum depth of penetration and is then retracted to the starting position are calculated by Eq. (18) from the equilibrium positions of the atoms as determined by the simulation results. Figures 2 and 3 provide contour subplots of the trace of the hydrostatic part of the stress tensor and the square root of the second invariant of the deviatoric part of the stress tensor, respectively. Note that each figure shows a top view and a profile view of a cross section through the indenter tip and parallel with the [010] plane at the maximum indentation depth and following unloading. Comparing the two figures, it can be seen that although the trace of the hydrostatic part of the stress tensor, i.e., that part which causes compression or dilation of the copper crystal, is almost recovered after unloading, a significant part of the deviatoric part of the stress tensor, i.e., that part which causes distortion of the copper crystal, is residual. This implies that the changes of the crystalline structure caused by the localized high stresses cause a distortion of the copper crystal. Furthermore, high residual stresses remain in the copper crystal after unloading.

Similarly, Eqs. (18) and (19) can be used to calculate the stresses and corresponding strains induced in the copper crystal at indenter displacement steps 12 and 21 [marked as

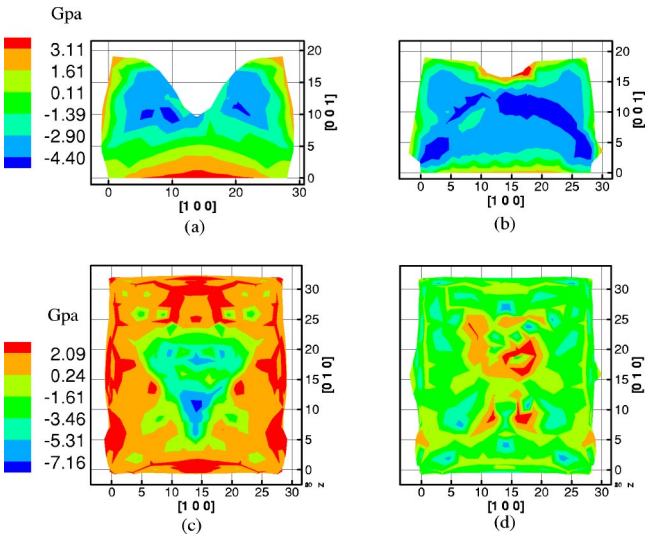

FIG. 2. The trace of the hydrostatic part of the atomic stress tensor at the maximum indentation depth and after unloading. Note that (a) and (b) present profile views of the cross sections through the indenter tip and parallel with the [010] plane, while (c) and (d) show top views (units are angstroms).

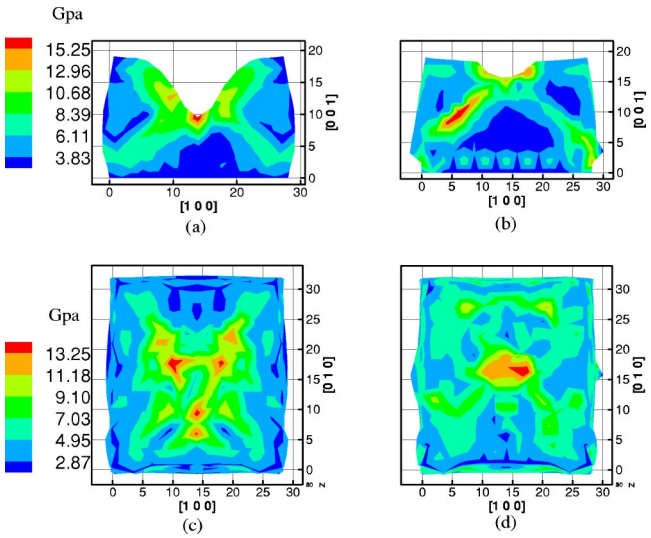

FIG. 3. The square root of the second invariant of the deviatoric part of the atomic stress tensor at the maximum indentation depth and after unloading. Note that (a) and (b) present profile views of the cross sections through the indenter tip and parallel with the [010] plane, while (c) and (d) show top views (units are angstroms).

point *A* in Fig. 1(b)] from the equilibrium positions of the atoms determined from the simulation results. Figures 4 and 5 present top-view contour subplots of the trace of the hydrostatic part and the square root of the second invariant of the deviatoric part of the stress tensor and the strain tensor, respectively, at displacement steps 12 and 21 of the simulation. Figures 4 and 5 show that the von Mises shear stress and the corresponding distortion strain have larger values in the region where dislocations emit along ⟨110⟩ directions. Therefore, we conclude that von Mises stress is a good indicator qualitatively and induces serious distortion that will be revealed by the strain tensor.

Figure 6 shows the spatial distribution of the slip vector norm $|s|$ at points *A* and *D* of the load-depth curve shown in Fig. 1(b). Note that Figs. 6(a) and 6(c) present isometric views, while Figs. 6(b) and 6(d) provide top views. From

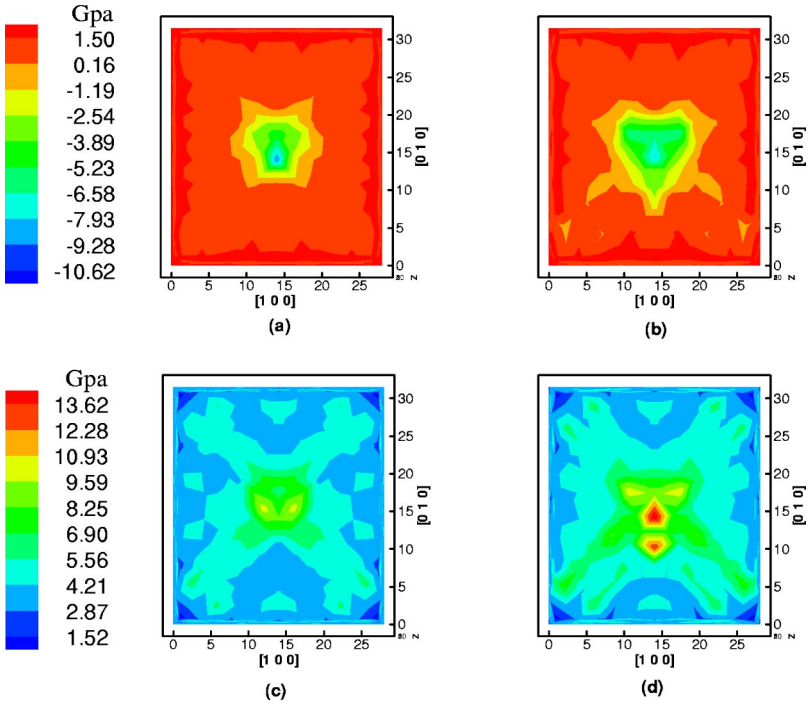

FIG. 4. Top-view contour subplots of the trace of the hydrostatic part and the square root of the second invariant of the deviatoric part of the atomic stress tensor at displacement steps 12 and 21 (units are angstroms).

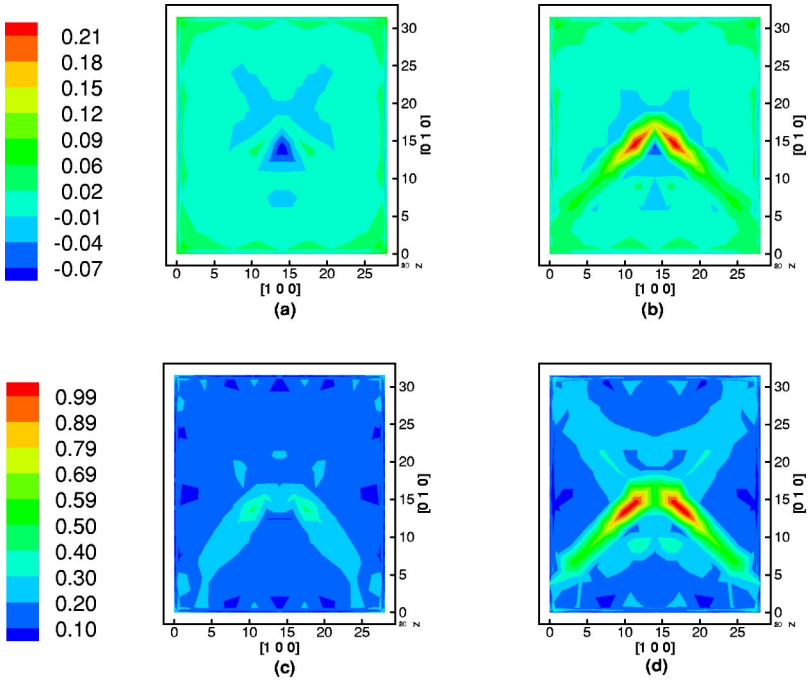

FIG. 5. Top-view contour subplots of the trace of the hydrostatic part and the square root of the second invariant of the deviatoric part of the atomic strain tensor at displacement steps 12 and 21 (units are angstrom).

these figures, it is clear that the dislocations are emitted from the indentation point along the ⟨110⟩ directions, and that the magnitude of their slip vectors is approximately $a_0/3\sqrt{2}$ (where a_0 denotes the Cu lattice parameter). Although a previous study has discussed the use of a scanning tunneling microscopy image to observe the dislocation emissions caused by the nanoindentation of an Au (001) surface,[12] it is important to emphasize that whether or not the emission of the dislocations can be observed depends upon the orientation of the surface and the geometry of the indenter.

In exploring the dislocation reactions which occur during

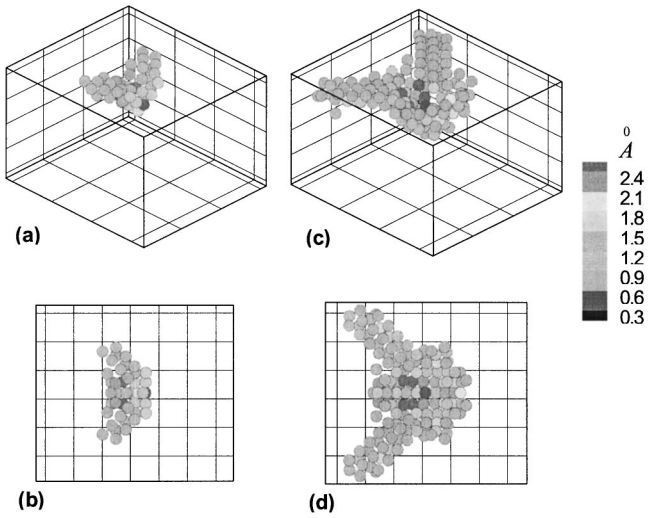

FIG. 6. Spatial distribution of the slip vector norm $|s|$ at point A and point D of the simulated load-depth curve presented in Fig. 1(a). Note that (a) and (c) present isometric views, while (b) and (d) show top views.

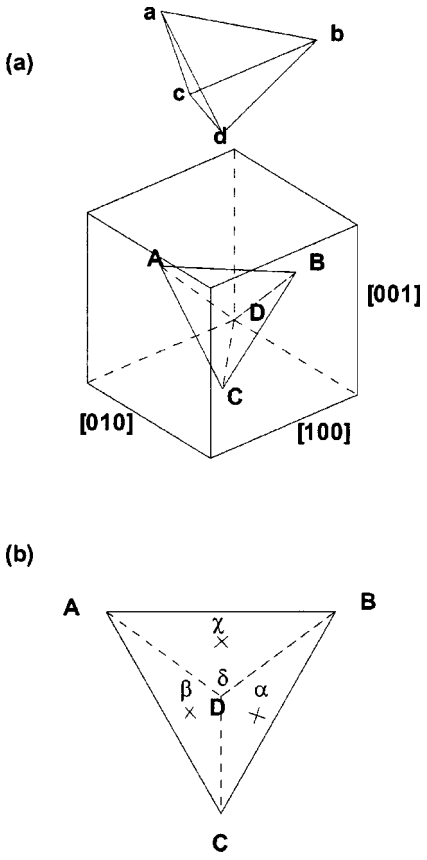

FIG. 7. (a) Tetrahedron *ABCD* formed by connecting the four nearest adjacent atoms in the face centered crystal. Tetrahedron *abcd* represents the indenter. (b) Thompson tetrahedron.

the nanoindentation of fcc metals, it is convenient to adopt the Thompson tetrahedron notation. From Fig. 7(a), it can be seen that the four different sets of {111} planes are parallel to the four faces of a regular tetrahedron whose edges are parallel to the ⟨110⟩ slip directions. As shown in the figure, the geometry of the indenter is illustrated by another nonregular tetrahedron. It can be seen that the apex and the triangular base of the indenter are inverted with respect to the surface, and that one side of its triangular base is parallel to the [100] direction.

As the indenter impresses into the surface, the *abd* plane of the indenter induces dislocation nucleation and glides along segment *CD* in the *ACD* and *BCD* planes. In terms of the Thompson tetrahedron notation illustrated in Fig. 7(b), the four corners of the tetrahedron are labeled by *A*, *B*, *C*, and *D*, while the midpoints of the four planes are labeled by α, β, γ, and δ. The perfect dislocation on the plane *ACD* would split in this plane with the reaction

$$CD \rightarrow C\alpha + \alpha D. \tag{24}$$

It is energetically favorite according to the description in Ref. 16 and therefore a reasonable conjecture in our static analysis.

The dissociation of the perfect dislocations on the *ACD* and *BCD* planes, respectively, induces a stair-rod dislocation along segment *CD* with a Burgers vector of $\alpha\beta$. This dislocation acts as a strong barrier to the subsequent glide of the dislocations. It is noted that the strain hardening which is evident in the simulated load-depth curve can be attributed to the progressive introduction of such barriers.

CONCLUSION

This study has presented the use of a modified-FEM approach to simulate the dislocation emissions which occur in a (001) Cu surface during a nanoindentation cycle. This method is based upon a nonlinear finite-element formation, and ignores the effects of atomic thermal vibration. In this way, the problem reduces to a quasistatic case, whose solution is far less computationally intensive than the traditional MD simulation approach. Slip vector analysis has been applied to explore the phenomenon of dislocation emissions induced by the nanoindentation of the (001) Cu surface. It has been suggested that these dislocations may explain the strain hardening effect observed in the simulated load-depth curve. Furthermore, the distribution of the stresses and corresponding strains has been examined in order to elucidate the atomic plastic behavior induced during the nanoindentation cycle. The results have indicated that the von Mises shear stress is a good indicator of the dislocation emissions observed in the simulation.

ACKNOWLEDGMENTS

The authors gratefully acknowledge the support by the National Science Council of Taiwan, under Grant No. NSC 91-2218-E-274-001, and the U.S. AFOSR under Contract No. F62562-03-P-0378.

[1] I. Adhihetty, J. Hay, W. Chen, and P. Padmanabhan, in *Fundamentals of Nanoindentation and Nanotribology*, edited by N. R. Moody, W. W. Gerberich, S. P. Baker, and N. Burnham, MRS Symposia Proceedings No. 522 (Materials Research Society, Pittsburgh, 1998), p. 317.
[2] B. N. Lucas, W. C. Oliver, and J. E. Swindeman (Ref. 1), p. 3.
[3] J. L. Hay, M. E. O'Hern, and W. C. Oliver (Ref. 1), p. 27.
[4] J. C. Hay and G. M. Pharr (Ref. 1), p. 39.
[5] E. Lugscheider, C. Barimani, and M. Lake (Ref. 1), p. 311.
[6] W. Lu and K. Komvopoulos, J. Tribol. **123**, 641 (2001).
[7] C. Klapperich, K. Komvopoulos, and L. Pruitt, J. Tribol. **123**, 624 (2001).
[8] B. Bhushan, *Handbook of Micro/Nano Tribology* (CRC, Boca Raton, FL, 1995).
[9] Y. Choi and S. Suresh, Acta Mater. **50**, 1881 (2002).
[10] Y. Choi and S. Suresh, Scr. Mater. **48**, 249 (2003).
[11] J. A. Zimmerman, C. L. Kelchner, P. A. Klein, J. C. Hamilton, and S. M. Foiles, Phys. Rev. Lett. **87**, 165507 (2001).
[12] O. R. de la Fuente, J. A. Zimmerman, M. A. Gonzalez, J. de la Figuera, J. C. Hamilton, W. W. Pai, and J. M. Rojo, Phys. Rev. Lett. **88**, 036101 (2002).
[13] A. Gannepalli and S. K. Mallapragada, Phys. Rev. B **66**, 104103 (2002).
[14] T. Inamura, H. Suzuki, and N. Takezawa, Int. J. Jpn. Soc. Precis. Eng. **25**, 259 (1991).
[15] M. F. Horstemeyer, M. I. Baskes, A. Godfrey, and D. A. Hughes, Int. J. Plast. **18**, 203 (2002).
[16] D. Hull and D. J. Bacon, *Introduction to Dislocations* (Pergamon, New York, 1984).